The Astrophysical Journal, 999:133 (11pp), 2026 March 1 https://doi.org/10.3847/1538-4357/ae3f99


# Broadband Timing and Spectral Study of Accreting Millisecond X-Ray Pulsar SAX J1808.4–3658 during Its 2022 Outburst

Rahul Sharma[1], Andrea Sanna[2], and Prince Sharma[3]
[1] Inter-University Centre for Astronomy and Astrophysics (IUCAA), Ganeshkhind, Pune 411007, India; rahul1607kumar@gmail.com
[2] Universitá degli Studi di Cagliari, Dipartimento di Fisica, SP Monserrato-Sestu, Km 0.7, 09042 Monserrato, Italy
[3] Department of Applied Sciences, UPES, Bidholi, Dehradun, Uttarakhand 248007, India
*Received 2025 October 8; revised 2026 January 9; accepted 2026 January 27; published 2026 February 27*

## Abstract

We report on our investigation of the NuSTAR and AstroSat observations along with simultaneous NICER observations of the accreting millisecond X-ray pulsar SAX J1808.4–3658, obtained during its tenth outburst from 2022. The NuSTAR observation captured the source near the outburst peak, while AstroSat observed it during the decay phase. Coherent pulsations at ∼401 Hz were detected throughout the outburst, with the fundamental amplitude in the 3–30 keV range increasing from ∼4% near the peak to ∼6% during the decay. The pulsations display strong energy dependence and negative time lags of ∼0.2–0.3 ms, with harder photons leading softer ones. The broadband spectra in both epochs are well described by a soft thermal component and Comptonized continuum, together with a prominent relativistic reflection component. As the outburst evolved, the continuum softened ($\Gamma$ increasing from ∼1.88 to ∼1.99) and the coronal electron temperature decreased ($kT_e$ from ∼31 to ∼18 keV), consistent with enhanced Compton cooling at lower accretion rates. The ionization parameter declined ($\log \xi$ from ∼3.4 to ∼1.8) while the reflection fraction increased, suggesting a changing accretion geometry with a more compact corona and a larger disk covering fraction during the decay phase. The X-ray luminosity decreased by a factor of ∼3 between the two epochs. Our results suggest the coupled evolution of the corona, disk, and magnetosphere as the mass accretion rate declines.

*Unified Astronomy Thesaurus concepts:* Low-mass x-ray binary stars (939); Neutron stars (1108); Millisecond pulsars (1062); Compact objects (288); Accretion (14)

## 1. Introduction

Accretion-powered millisecond X-ray pulsars (AMXPs) form a special class of neutron star low-mass X-ray binaries (NS-LMXBs) where an old NS in a compact binary is accelerated to very high spin due to accretion from its companion. The spin period in such systems is observed to be in the range of milliseconds (G. Srinivasan 2010). SAX J1808.4–3658 is the first LMXB discovered to show millisecond X-ray pulsations with a spin frequency of ∼401 Hz in a compact binary with an orbital period of ∼2 hr (D. Chakrabarty & E. H. Morgan 1998; R. Wijnands & M. van der Klis 1998). Currently, a total of 24 sources have been identified and cataloged that shows millisecond pulsations (e.g., M. Ng et al. 2021; A. Patruno & A. L. Watts 2021; P. Bult et al. 2022; T. Di Salvo & A. Sanna 2022; A. Sanna et al. 2022a).

Several studies suggest that the magnetic field of AMXPs ranges between $\sim 10^8$ and $10^9$ G (see, e.g., D. Mukherjee et al. 2015; R. M. Ludlam et al. 2017; R. Sharma et al. 2020). Although relatively weak, such a field proves strong enough to channel the accreting material onto the magnetic poles, resulting in X-ray modulation at the spin frequency. Spectral properties of AMXPs typically show the characteristics of thermal emission from the accretion disk and/or NS surface, thermal Comptonization, and reprocessed emission from the accretion disk in the form of a reflection spectrum (e.g., A. Papitto et al. 2009; E. M. Cackett et al. 2010; R. Sharma et al. 2019; T. Di Salvo & A. Sanna 2022). These systems are often observed in the hard spectral state, although some studies caught these sources in transition states between the hard and soft states (R. Sharma et al. 2019; T. Di Salvo & A. Sanna 2022; A. Beri et al. 2023), similar to those seen in atoll sources (e.g., G. Hasinger & M. van der Klis 1989).

Since its discovery, SAX J1808.4–3658 has exhibited recurrent outbursts every 2.5–4 yr. To date, 11 such events have been recorded: in 1996, 1998, 2000, 2002, 2005, 2008, 2011, 2015, 2019, 2022, and 2025, the largest number of known outbursts for any AMXP (T. Di Salvo & A. Sanna 2022; G. Illiano et al. 2023; D. M. Russell et al. 2025). Owing to this frequent activity, SAX J1808.4–3658 has been the subject of extensive multiwavelength investigations, spanning quiescence to outburst phases across radio, optical, UV, and X-ray bands (e.g., A. Patruno et al. 2017; M. C. Baglio et al. 2020; A. J. Goodwin et al. 2020; F. Ambrosino et al. 2021; R. Sharma et al. 2023).

This work focuses on the 2022 outburst of SAX J1808.4–3658, which began around 2022 August 19 (Y. Imai et al. 2022; A. Sanna et al. 2022b). About five days after its onset, the flux started to decline, and the source subsequently entered the characteristic reflaring stage that marks the late phases of its outbursts, which lasted for more than a month (M. C. Baglio et al. 2022; G. Illiano et al. 2022). At peak, the 0.6–10 keV luminosity reached $\simeq 1 \times 10^{36}$ erg s$^{-1}$. The 2022 event displayed a somewhat unusual outburst profile compared to the typical behavior of SAX J1808.4–3658: the normally short-lived peak persisted for the longest duration recorded so far, while the slow-decay/rapid-drop phase was noticeably shorter (∼10–15 days) than usual (G. Illiano et al. 2023). The Neutron Star Interior Composition Explorer (NICER;

**Table 1**
Log of X-Ray Observations of SAX J1808.4–3658 Analyzed in This Work.

| Epoch | Instrument | obsID | Start Time | | Stop Time | | Exposure (ks) |
|---|---|---|---|---|---|---|---|
| | | | (yy-mm-dd hh:mm:ss) | MJD | (yy-mm-dd hh:mm:ss) | MJD | |
| 1 | NuSTAR | 80701312002 | 2022-08-22 17:36:31 | 59813.73369 | 2022-08-25 04:16:06 | 59816.17785 | 107 |
| | NICER-1 | [a] | 2022-08-22 18:38:10 | 59813.77650 | 2022-08-24 20:14:26 | 59815.84335 | 20 |
| 2 | AstroSat/LAXPC | 9000005318 | 2022-08-26 08:00:39 | 59817.33379 | 2022-08-27 13:59:59 | 59818.58332 | 50 |
| | AstroSat/SXT | 9000005318 | 2022-08-26 08:24:57 | 59817.35066 | 2022-08-27 13:55:01 | 59818.57988 | 27 |
| | NICER-2 | [b] | 2022-08-26 10:20:36 | 59817.43097 | 2022-08-27 13:20:26 | 59818.55585 | 9.4 |

**Notes.**
[a] Observation covers snapshots from obsIDs 5050260104, 5050260105, 5574010101, 5574010102, and 5050260106.
[b] Observation covers snapshots from obsIDs 5574010104 and 5574010105.

K. C. Gendreau et al. 2016) tracked the outburst from its onset through the reflaring phase. Using these NICER data, G. Illiano et al. (2023) carried out a coherent timing analysis, reporting a secular spin-down of the pulsar at a rate of $1.15(6) \times 10^{-15}\,\mathrm{Hz\,s^{-1}}$. They also found evidence for a decrease in the orbital period, with the orbital phase epochs exhibiting an ∼11 s modulation consistent with a ∼21 yr periodicity.

In addition to the NICER monitoring, the 2022 outburst was also followed up with Nuclear Spectroscopic Telescope Array (NuSTAR) and AstroSat near the peak and the decay phase of the outburst, respectively. Recently, A. Kaushik et al. (2025) reported the evolution of spectral and aperiodic timing properties using NICER and AstroSat. K. Bruce et al. (2026) reported a broadband spectral study with NICER+NuSTAR observations comparing the 2019 and 2022 outbursts. In this work, we utilized the NICER, NuSTAR, and AstroSat observations to investigate the pulse timing and spectral properties of SAX J1808.4–3658 across a broad energy range during the peak and the decay phase of the 2022 outburst. The structure of the paper is as follows: Section 2 describes the data reduction and analysis techniques. The timing and spectral analysis results are summarized in Section 3. We discuss our findings in Section 4 and conclude in Section 5.

## 2. Observation and Data Analysis

The observations used in this work are detailed in Table 1.

### 2.1. NuSTAR

The NuSTAR (F. A. Harrison et al. 2013) mission comprises two telescopes that focus X-rays between 3 and 78 keV onto two identical focal planes (usually called focal plane modules A and B, or FPMA and FPMB).

For this work, we have used the most recent NuSTAR analysis software distributed with HEASOFT version 6.34 and the latest calibration files (v20250122) for reduction and analysis of the NuSTAR data. The calibrated and screened event files have been generated by using the task NUPIPELINE. A circular region of radius 70″ centered at the source position was used to extract the source events. Background events were extracted from a circular region of the same size away from the source. The task NUPRODUCT was used to generate the light curves, spectra, and response files. The FPMA and FPMB light curves were background-corrected and summed using LCMATH. The spectra were grouped using FTGROUPPHA by following the J. S. Kaastra & J. A. M. Bleeker (2016) optimal binning scheme with a minimum of 25 counts per bin.

### 2.2. AstroSat

AstroSat is India's first dedicated multiwavelength astronomy satellite (P. C. Agrawal 2006; K. P. Singh et al. 2014), launched in 2015. It has five principal payloads on board: (i) the Soft X-ray Telescope (SXT), (ii) the Large Area X-ray Proportional Counters (LAXPCs), (iii) the Cadmium–Zinc–Telluride Imager, (iv) the Ultra-Violet Imaging Telescope, and (v) the Scanning Sky Monitor. In this work, we have only analyzed data from SXT and LAXPC.

#### 2.2.1. LAXPC

LAXPC is one of the primary instruments aboard AstroSat. It consists of three coaligned identical proportional counters (LAXPC10, LAXPC20, and LAXPC30) that work in the energy range 3–80 keV. Each LAXPC detector independently records the arrival time of each photon with a time resolution of 10 μs and has five layers (for details see J. S. Yadav et al. 2016; H. M. Antia et al. 2017).

As LAXPC10 was operating at low gain and detector LAXPC30[4] was switched off during the observation, we used only the LAXPC20 detector for our analysis. We used the data collected in the event analysis mode and processed them using the LAXPCSOFT[5] v3.4.4 software package to extract light curves and spectra. LAXPC detectors have a dead-time of 42 μs, and the extracted products are dead-time-corrected. The background in LAXPC is estimated from the blank-sky observations (see H. M. Antia et al. 2017 for details). To minimize the background, we have performed all analyses using the data from the top layer (L1, L2) of the LAXPC20 detector. We have used corresponding response files to obtain channel-to-energy conversion information while performing energy-resolved analysis.

#### 2.2.2. SXT

SXT is a focusing X-ray telescope with a CCD in the focal plane that can perform X-ray imaging and spectroscopy in the 0.3–7 keV energy range (K. P. Singh et al. 2016, 2017). SAX J1808.4–3658 was observed in the photon counting (PC) mode

[4] LAXPC30 has been switched off since 2018 March 8 due to abnormal gain changes; see http://astrosat-ssc.iucaa.in/.
[5] http://www.tifr.res.in/~astrosat_laxpc/LaxpcSoft.html

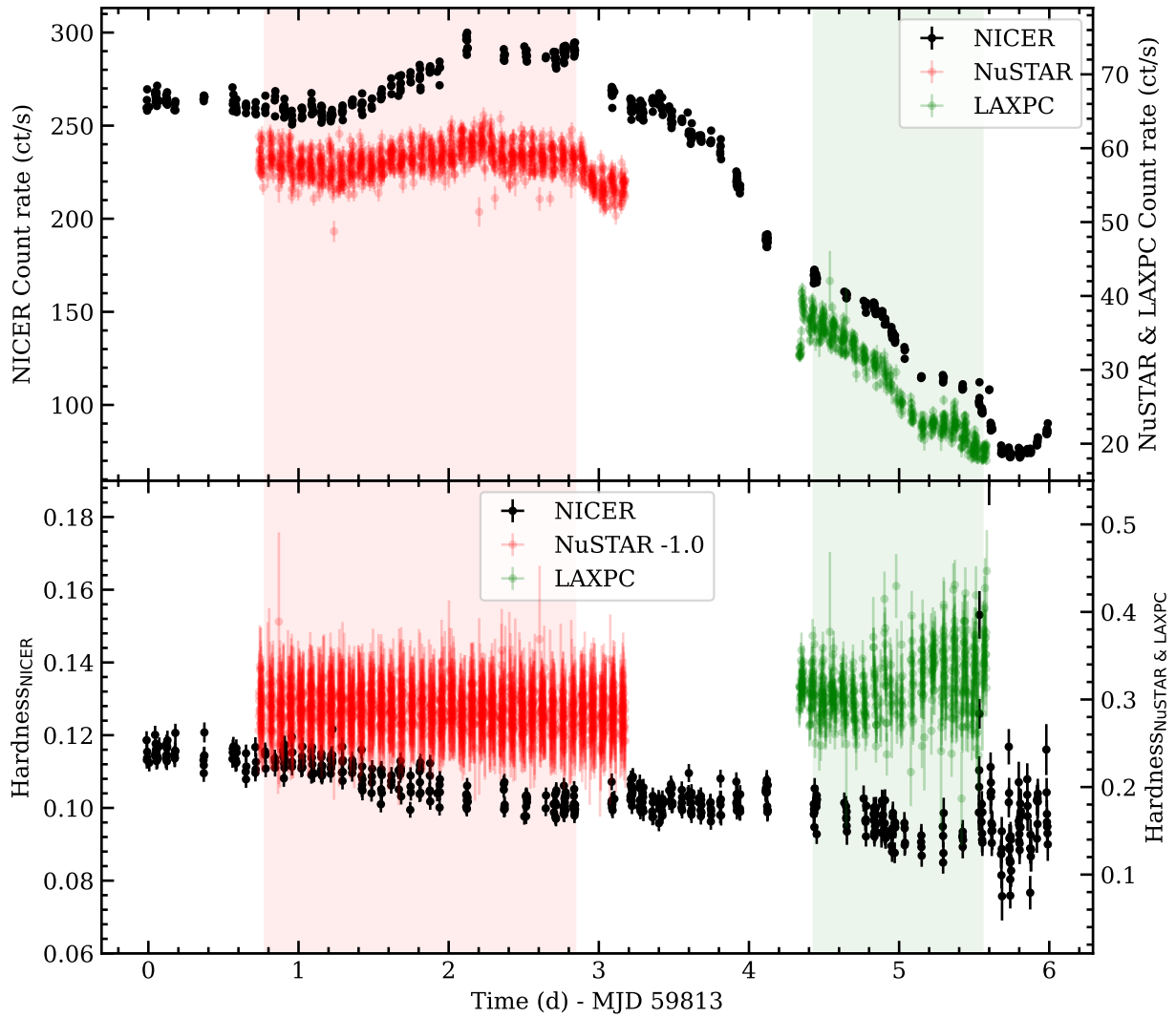


**Figure 1.** The light curve of SAX J1808.4–3658 during its 2022 outburst obtained with NICER, NuSTAR, and AstroSat/LAXPC binned at 100 s in the energy ranges 0.5–10 keV, 3–30 keV, and 3–30 keV, respectively. The lower panel shows the hardness ratio, defined as the count-rate ratios between 3–10 and 0.5–3 keV for NICER, and between 10–30 and 3–10 keV for NuSTAR and AstroSat/LAXPC. The hardness values for NuSTAR have been shifted by −1 to match LAXPC. The shaded region marks the NICER segment that was combined for further analysis.

with SXT. Level 1 data were processed with `AS1SXTLevel2-1.4b` pipeline software to produce level 2 clean event files. The level 2 cleaned files from individual orbits were merged using the SXT event merger tool.[6] The merged event file was then used to extract images and spectra using the XSELECT task, provided as part of HEASOFT v6.31.1. A circular region with a radius of 16′ centered on the source was used. No source pileup was observed as the count rate was below the threshold limit for pileup (<40 counts $s^{-1}$) in the PC mode.[7] For spectral analysis, we have used the blank-sky SXT spectrum as background (SkyBkg_sxt_LE0p35_R16p0_v05_Gd0to12.pha) and the spectral redistribution matrix file (sxt_pc_mat_g0to12.rmf) provided by the SXT team.[8] We generated the correct off-axis auxiliary response files (ARF) using the sxtARFModule tool from the on-axis ARF (sxt_pc_excl00_v04_20190608.arf) provided by the SXT instrument team.

[6] https://github.com/gulabd/SXTMerger.jl
[7] https://www.tifr.res.in/~astrosat_sxt/instrument.html
[8] http://www.tifr.res.in/~astrosat_sxt/dataanalysis.html

### 2.3. NICER

NICER (K. C. Gendreau et al. 2016) is an X-ray telescope deployed on the International Space Station (ISS) in 2017 June. NICER X-ray Timing Instrument has 56 aligned FPMs, each made up of an X-ray concentrator optic associated with a silicon drift detector. It has a large effective area and high temporal resolution in the soft X-ray band. Each NICER observation typically comprises multiple short-duration pointings of the source, called snapshots, primarily driven by ISS orbit and visibility constraints.

NICER monitored SAX J1808.4–3658 after the onset of the outburst from MJD 59810 to 59883. NICER data were processed with HEASOFT v6.34 and the NICER Data Analysis Software (`nicerdas`) v2024-08-18_V013, using Calibration Database (CALDB) xti20240206. Standard calibration and screening criteria were applied using the `nicerl2` tool. The NICER campaign overlapped quasi-simultaneously with the NuSTAR and AstroSat observations. Since individual NICER observations typically spanned less than a day, we merged segments overlapping with NuSTAR and AstroSat using `niobsmerge` (Figure 1). NICER-1 contains snapshots of

obsIDs 5050260104, 5050260105, 5574010101, 5574010102, and 5050260106, while NICER-2 covers obsIDs 5574010104 and 5574010105 (see Table 1). The merged event files were then used to extract light curves with `nicerl3-lc` and spectra with `nicerl3-spect`. Background contributions were estimated using the `nibackgen3C50` tool (R. A. Remillard et al. 2022).

All photon arrival times were corrected to the solar system barycentre using AS1BARY[9] for AstroSat/LAXPC and BARYCORR for NuSTAR and NICER, adopting the JPL DE405 planetary ephemeris. For NuSTAR, we used the latest clock correction file available with the calibration database v20250122. The source position used for the corrections was R.A. (J2000) = $18^{h}08^{m}27\overset{s}{.}647$ and decl. (J2000) = $-36°58'43\overset{''}{.}90$ (P. Bult et al. 2020).

## 3. Results

### 3.1. Light Curve

Figure 1 shows the light curve of SAX J1808.4–3658 during its 2022 outburst as obtained with NICER, NuSTAR, and AstroSat/LAXPC, binned at 100 s in the energy ranges 0.5–10 keV, 3–30 keV, and 3–30 keV, respectively. The NuSTAR observation was carried out near the peak of the outburst, while the AstroSat observation took place during the decay phase. The shaded region marks the NICER segment that was merged with respect to NuSTAR and AstroSat observations. These two observations are hereafter referred to as Epochs 1 and 2, respectively. The bottom panel of Figure 1 shows the hardness ratio computed from light curves in the two energy bands 3–10 and 0.5–3 keV for NICER, and between 10–30 and 3–10 keV for NuSTAR and AstroSat/LAXPC. During the NICER monitoring, the hardness ratio exhibits a slight decreasing trend over time. A more pronounced change is observed between the two epochs, with the hardness ratio decreasing from ∼1.3 during the NuSTAR observation to ∼0.3 during the AstroSat observation, indicating significant spectral softening as the outburst evolved. Although the AstroSat and NICER-2 observation shows clear flux evolution, no significant hardness variations were detected in either epoch, suggesting that the source did not undergo a spectral state transition within these intervals.

### 3.2. Timing Analysis

Pulses from a rotating NS can lose coherence on relatively short timescales due to Doppler modulation of the photon arrival times in the short ∼2 hr orbit. In addition, the low pulse fraction makes it challenging to detect pulsations. To recover the pulsations and measure the true spin frequency during these observations, the photon arrival times must be corrected for binary motion. The time delay induced by the orbital motion, assuming a circular (or very low eccentricity) orbit, is given by (L. Burderi et al. 2007)

$$\frac{z(t)}{c} = \frac{a_x \sin i}{c} \sin\left(\frac{2\pi}{P_{\rm orb}}(t - T^{\star})\right), \quad (1)$$

where $a_x \sin i/c$ is the projected semimajor axis of the neutron star orbit in light-seconds, $P_{\rm orb}$ is the orbital period, and $T^{\star}$ is the time of passage through the ascending node.

[9] http://astrosat-ssc.iucaa.in/?q=data_and_analysis

**Table 2**
Spin Frequency and Fractional Amplitude

| Instrument | Spin Frequency (Hz) | Fractional Amplitude (%) | |
|---|---|---|---|
| | | Fundamental | Harmonic |
| NuSTAR | 400.9752098 (1) | 4.06 (11) | 1.71 (11) |
| NICER-1 | 400.9752096 (1) | 4.44 (6) | 0.80 (6) |
| AstroSat | 400.9752096 (2) | 6.32 (16) | 1.72 (16) |
| NICER-2 | 400.9752089 (3) | 6.54 (7) | 0.26 (7) |

The most recent orbital solution, derived from NICER observations during the 2022 outburst, was reported by G. Illiano et al. (2023). We therefore corrected the photon arrival times of the observations used using this updated ephemeris. To search for pulsations, we applied epoch-folding around the spin frequency $\nu_0 = 400.97520953$ Hz, as measured during the same outburst with NICER monitoring (G. Illiano et al. 2023). The signal was sampled with 16 phase bins, and the frequency space was explored in steps of $10^{-8}$ Hz over 10,001 trials. The most significant pulse profile was obtained for an average local spin frequency ($\bar{\nu}$), which is listed in Table 2 for each dataset used. The uncertainty on $\bar{\nu}$ was estimated using Monte Carlo simulations with 1000 synthetic realizations of the data. Starting from the observed event list and good time intervals, we folded the events at the best frequency to obtain a pulse profile. This profile was then used as a template to generate synthetic event lists that preserve the source variability and observational gaps. Each synthetic event list was subjected to an independent frequency search using the epoch-folding statistic. The resulting distribution of best-fit frequencies from the 1000 trials was used to determine the statistical uncertainty on $\bar{\nu}$.

Since the orbital solution is already well constrained by long-term NICER monitoring, and no spin frequency derivative was detected during the 2022 outburst (G. Illiano et al. 2023), we assumed $\bar{\nu}$ to represent the true spin frequency for each observation. We also attempted to track pulse phase delays following the method of R. Sharma et al. (2023), but found no significant evidence for deviations from the orbital solution of G. Illiano et al. (2023).

Figure 2 presents the pulse profile of SAX J1808.4–3658, obtained by epoch-folding the NICER, NuSTAR, and AstroSat/LAXPC datasets at $\bar{\nu}$ into 16 phase bins in the energy ranges 0.5–10 keV, 3–30 keV, and 3–30 keV, respectively. The pulse shape is well described by the sum of two harmonically related sinusoidal functions with background-corrected fractional amplitude of the fundamental and harmonic components listed in Table 2. The fractional amplitude for the fundamental increases from ∼4% in Epoch 1 to ∼6% in Epoch 2 across the broad energy range. For the harmonic, the amplitude remains nearly constant in the 3–30 keV band, but decreases in the 0.5–10 keV band, from 0.8% in Epoch 1 to 0.26% in Epoch 2. A third harmonic is marginally detected in the 3–30 keV band with a fractional amplitude of ∼0.3%, although its significance is low, with F-test false-alarm probabilities of 0.01 and 0.05 for Epochs 1 and 2, respectively.

We then investigated the energy dependence of the pulse amplitude and phase. The full dataset was divided into different energy bands, and each was epoch-folded at $\bar{\nu}$. The resulting pulse profiles were fitted with two harmonically related sinusoidal functions. Figure 3 (top panels) shows the

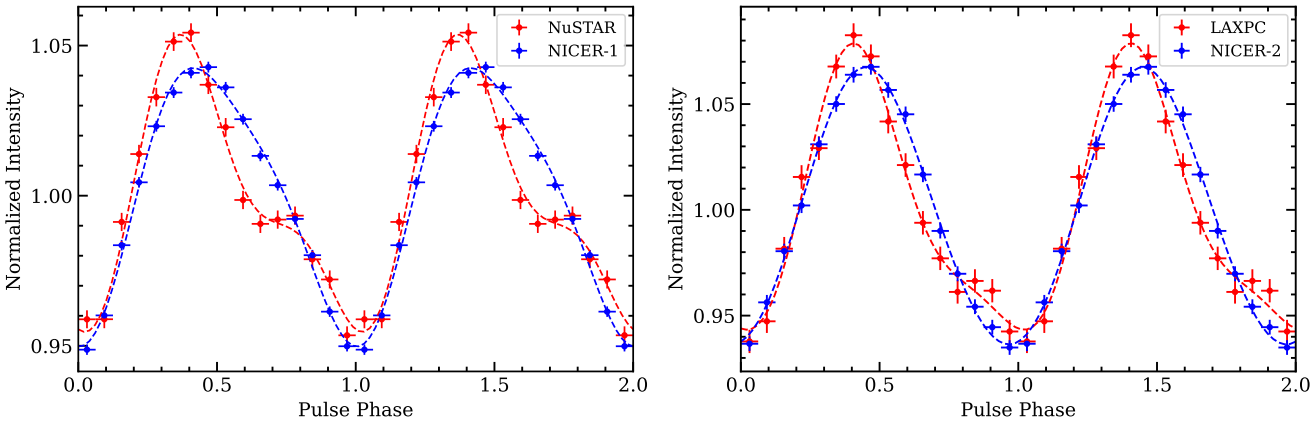


**Figure 2.** Pulse profiles of SAX J1808.4–3658 from two observing epochs, obtained by epoch-folding the data with spin frequencies listed in Table 2 after correcting for the orbital motion. Left panel: Epoch 1, showing profiles in the 0.5–10 keV band from NICER and in the 3–30 keV band from NuSTAR. Right panel: Epoch 2, showing profiles in the 0.5–10 keV band from NICER and in the 3–30 keV band from AstroSat/LAXPC. The solid lines denote the best-fitting model, which is the superposition of two sinusoidal functions with harmonically related periods. For clarity, two pulse cycles are shown.

variation of background-corrected fractional amplitude of the fundamental and harmonic components, with Epoch 1 on the left and Epoch 2 on the right. In both epochs, the fractional amplitude of the fundamental and harmonic was found to be energy-dependent. The fundamental component showed an increase up to 3 keV and then a decreasing trend at higher energies for both epochs. The peak fractional amplitude of the fundamental reached ∼7% in Epoch 1 and was higher in Epoch 2 at ∼9%. The harmonic component in Epoch 1 increased steadily with energy, reaching ∼2% at the higher energies. In Epoch 2, however, the harmonic was not significantly detected at low energies (below 5 keV, ∼0.5%) but showed a rising trend above 5 keV, reaching ∼3% at higher energies.

The bottom panels of Figure 3 show the energy dependence of the time lag, derived from the phase lag, for the fundamental and harmonic components. In Epoch 1, the fundamental component exhibited no significant lag below 3 keV, while at higher energies it showed a negative lag, reaching ∼0.25 ms and indicating that the hard photons arrive earlier than the soft photons. The harmonic component in this epoch showed no clear lag, except for a negative lag around 2 keV. In Epoch 2, the fundamental component again displayed a negative lag above 3 keV, consistent with Epoch 1. However, unlike Epoch 1, the harmonic component in Epoch 2 exhibited a negative lag of ∼0.2 ms above 3 keV, while no significant trend was observed below 3 keV owing to its low detection significance.

### 3.3. Spectral Analysis

For both epochs, NuSTAR (FPMA and FPMB) and AstroSat (SXT and LAXPC) were fitted with the simultaneous NICER observations. We performed spectral fitting using XSPEC v12.14.1 (K. A. Arnaud 1996) with the component `tbabs` to model interstellar neutral hydrogen absorption (J. Wilms et al. 2000). We have added a constant to account for the cross-calibration between multiple instruments during simultaneous fitting. As the NICER spectra showed some systematic emission feature at 1 keV, which was not observed with SXT, we restricted the NICER spectral fitting to 1.2–10 keV. We also applied a gain correction for the SXT. The gain slope was fixed to 1.0, and the offset was allowed to vary. The gain offset was found to be ∼24 eV. A systematic uncertainty of 1% was added to SXT and LAXPC spectra (H. M. Antia et al. 2017). All uncertainties and limits in this paper for spectral analysis correspond to a 90% confidence level.

The broadband continuum of Epoch 1 can be well described by a combination of a soft thermal component and thermal Comptonization. We modeled the soft emission with the `bbodyrad` model in XSPEC and the Comptonized continuum with `nthcomp` (A. A. Zdziarski et al. 1996). This model, however, provides a statistically unacceptable fit ($\chi^2$/dof = 1035/614) and exhibited prominent residuals around 6–7 keV (Figure 4), indicative of Fe K emission (e.g., E. M. Cackett et al. 2009; A. Papitto et al. 2009; T. Di Salvo et al. 2019), as well as a residual near 1.7 keV in the NICER data, likely associated with Si K calibration uncertainties. Adding a Gaussian emission line significantly improved the fit ($\chi^2$/dof = 603/611), yielding a centroid energy of 6.2 ± 0.2 keV, a broad line width of 1.0 ± 0.1 keV, and an equivalent width of 0.16 ± 0.03 keV. Including a second Gaussian component at 1.7 keV led to only a marginal improvement ($\Delta\chi^2 \sim 8$ for three additional degrees of freedom) with an equivalent width of ∼15 eV, and it was therefore excluded from subsequent modeling. The best-fit continuum corresponds to a blackbody temperature of ∼0.64 keV and a Comptonizing corona with photon index of $\Gamma \sim 1.86$, electron temperature of $kT_e \sim 27$ keV, and seed photon temperature of ∼0.2 keV, likely originating from the inner accretion disk.

The presence of the broad emission line (see Figure 4) motivated the inclusion of a self-consistent reflection model (A. C. Fabian & R. R. Ross 2010). We therefore employed the `relxillCP` model (J. A. García et al. 2018) of the `relxill` package v2.4 (T. Dauser et al. 2014; J. García et al. 2014). This physical model accounts for relativistic reflection from an incident `nthcomp` continuum. It can describe both the illuminating and reflected emission. The key parameters include the photon index ($\Gamma$), the accretion disk ionization parameter ($\log \xi$), disk density ($\log N$), inclination angle ($i$), inner and outer disk radii, reflection fraction ($\mathrm{refl_{frac}}$), and iron abundance relative to solar ($A_{\mathrm{Fe}}$). We adopted a single emissivity profile with $q = 3$ (E. M. Cackett et al. 2010; D. R. Wilkins & A. C. Fabian 2012) and fixed the outer disk radius at $R_{\mathrm{out}} = 1000R_G$, where $R_G$ is the gravitational radius, since the fit is not sensitive to larger values. The dimensionless

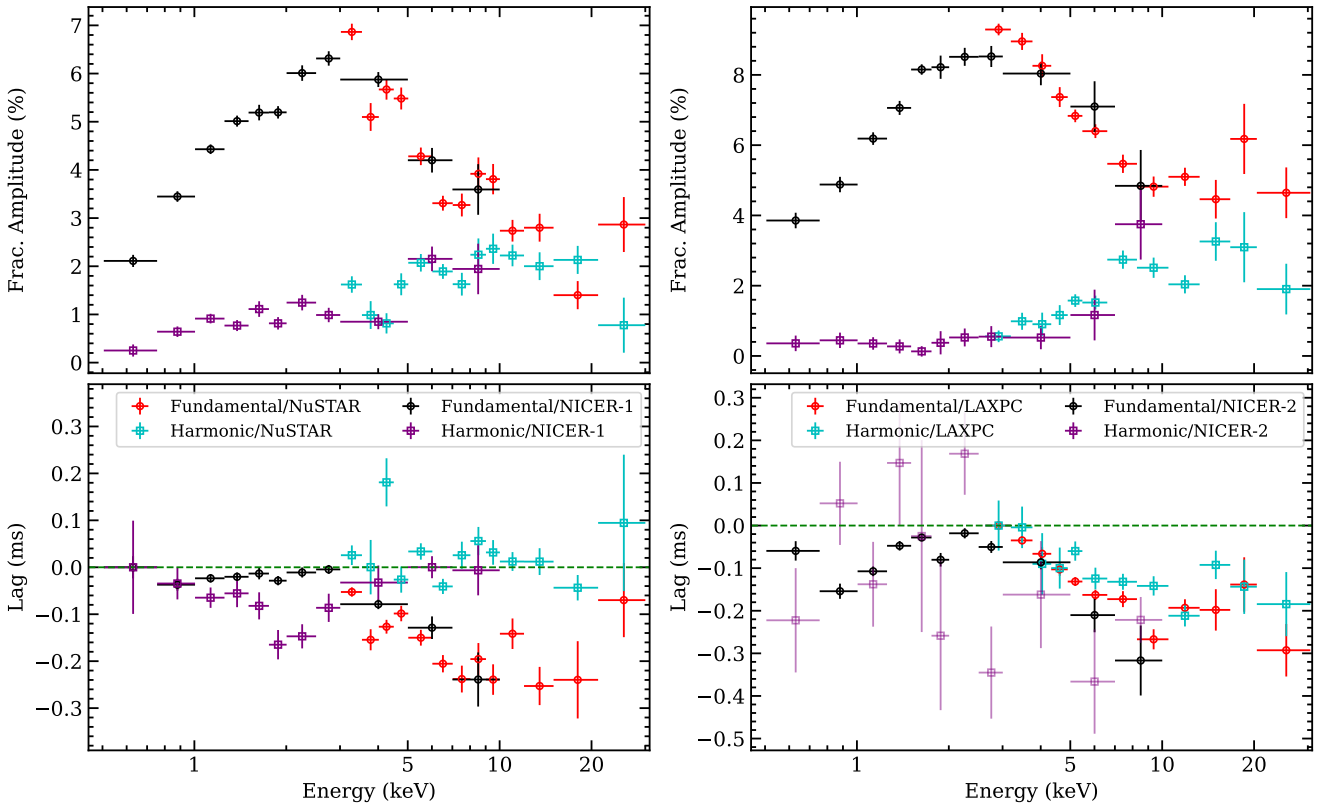


**Figure 3.** Energy-resolved pulse properties of SAX J1808.4–3658. Top panels: fractional amplitudes of the fundamental and harmonic components as a function of energy. Bottom panels: corresponding time lags of the fundamental and harmonic components. The left plots correspond to Epoch 1, with the zero lag defined relative to the pulse phase at 0.5 keV, while the right plots correspond to Epoch 2, with the zero lag defined at 3 keV.

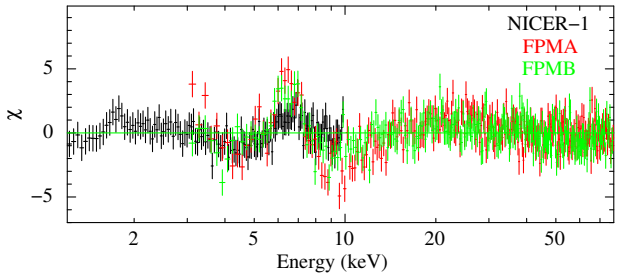


**Figure 4.** Residuals obtained after modeling the spectrum with an absorbed blackbody and Comptonization model. These residuals indicate the broad emission feature at 6–7 keV.

spin parameter $a$ was fixed at 0.1885, derived from the spin frequency $\nu = 401$ Hz using the relation $a = 0.47/P_{\rm ms}$, where $P_{\rm ms}$ is the spin period in milliseconds (T. M. Braje et al. 2000).

The NICER+NuSTAR spectrum was self-consistently described using the `tbabs*(bbodyrad+rexillCP)` model. This model yielded $\chi^2/{\rm dof} = 592.5/610$, indicating a good fit and accounting for the residuals in the 6–7 keV band. The best-fit spectrum is shown in the left panel of Figure 5 and the corresponding spectral parameters are listed in Table 3. During the fitting process, however, we encounter a degeneracy where another local minimum was found corresponding to a truncated inner disk radius at $12\,R_{\rm ISCO}$ and a nearly neutral reflector ($\log\xi \lesssim 0$). To avoid this degeneracy, we fixed the inner disk radius at the ISCO ($R_{\rm in} = R_{\rm ISCO}$). The preferred solution suggests moderately ionized reflection ($\log\xi \sim 3.4$), an inclination of 31°, and a poorly constrained iron abundance, with only a lower limit of $A_{\rm Fe} \gtrsim 2$, consistent with previous findings during the 2015 outburst (T. Di Salvo et al. 2019).

The same model also adequately describes the Epoch 2 spectrum (NICER+AstroSat; Table 3, right panel of Figure 5). The spectral parameters show notable differences between Epoch 1 and Epoch 2. Between the two epochs, the blackbody temperature remained nearly constant at ∼0.6 keV, but its normalization decreased, implying an apparent reduction in the emission region. The Comptonized continuum softened, with the photon index increasing from $\Gamma \sim 1.88$ in Epoch 1 to $\Gamma \sim 1.95$ in Epoch 2, and the electron temperature dropping from ∼32 to ∼15 keV, consistent with enhanced Compton cooling during the decay phase.

The relativistic reflection parameters also evolved. The inclination was found to be ∼48° in Epoch 2 compared to ∼31° in Epoch 1, though this may reflect modeling degeneracies. Previous studies have suggested even higher inclinations (>50°; E. M. Cackett et al. 2009; A. Papitto et al. 2009; T. Di Salvo et al. 2019). The inner disk radius remained unconstrained, with an upper limit of $R_{\rm in} < 2.2R_{\rm ISCO}$. The ionization parameter decreased significantly from $\log\xi \sim 3.4$ to $\log\xi \sim 1.8$, and the iron abundance in Epoch 2 was also poorly constrained, with only a lower limit of $A_{\rm Fe} > 4.6$.

Finally, we performed a joint spectral fit of Epochs 1 and 2 by linking parameters expected to remain constant across epochs. We linked the absorption column density, inclination, iron abundance, and disk density. The resulting best-fit spectra and model components are shown in Figure 6, and the best-fit spectral parameters are reported in Table 3. The joint fit yields results consistent with those from the individual fits, with $N_{\rm H} = 2.4 \times 10^{21}\,{\rm cm}^{-2}$. The continuum softens as the outburst

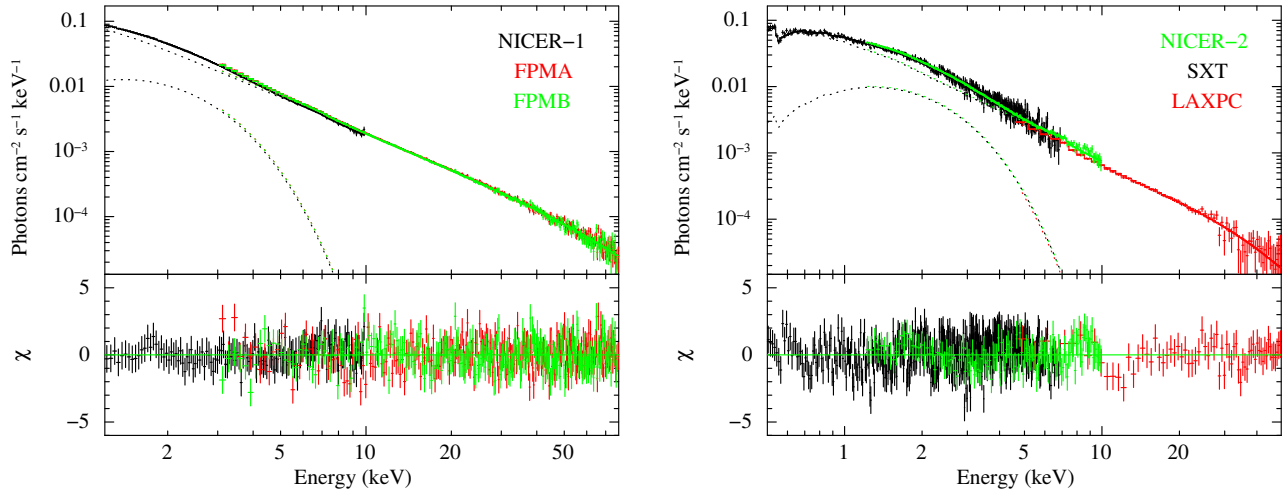


**Figure 5.** Best-fit broadband energy spectra from Epoch 1 (left) and 2 (right) using NICER+NuSTAR and NICER+SXT+LAXPC, respectively, fitted with the combined model `tbabs*(bbodyrad + relxillCP)`. The lower panels show residuals from the best-fit model.

**Table 3**
Best-fit Spectral Parameters of SAX J1808.4–3658 with Spectral Model `tbabs*(bbodyrad + relxillCP)`

| Parameters | Epoch 1 NICER+NuSTAR | Epoch 2 NICER+AstroSat | Joint Fit | | |
|---|---|---|---|---|---|
| | | | Epoch 1 | | Epoch 2 |
| $N_{\rm H}$ ($10^{21}$ cm$^{-2}$) | $2.9^{+0.6}_{-0.2}$ | $2.2 \pm 0.1$ | | $2.41 \pm 0.15$ | |
| $kT_{\rm BB}$ (keV) | $0.60 \pm 0.01$ | $0.57 \pm 0.01$ | $0.63 \pm 0.01$ | | $0.576 \pm 0.014$ |
| Norm | $77 \pm 9$ | $52 \pm 7$ | $63 \pm 6$ | | $46 \pm 6$ |
| $R_{\rm BB}$ (km)[a] | $3.1 \pm 0.2$ | $2.5 \pm 0.2$ | $2.8 \pm 0.1$ | | $2.4 \pm 0.2$ |
| Incl. (deg) | $31.3^{+3.6}_{-6.4}$ | $48.3^{+5.7}_{-2.1}$ | | $39.3^{+3.6}_{-1.9}$ | |
| $R_{\rm in}$ ($R_{\rm ISCO}$) | $1^{\rm fixed}$ | $<2.2$ | $1^{\rm fixed}$ | | $<3.1$ |
| $\Gamma$ | $1.88 \pm 0.01$ | $1.95^{+0.02}_{-0.01}$ | $1.88 \pm 0.01$ | | $1.99 \pm 0.03$ |
| log $\xi$ | $3.4^{+0.2}_{-0.3}$ | $1.87^{+0.24}_{-0.13}$ | $3.4 \pm 0.2$ | | $1.85^{+0.45}_{-0.15}$ |
| log($N$/cm$^{-3}$) | $18.0^{+1.6}_{\rm pegged}$ | $16.9^{+0.3}_{\rm pegged}$ | | $17.0^{+0.8}_{\rm pegged}$ | |
| $A_{\rm Fe}$ | $>2.0$ | $>4.6$ | | $3.3 \pm 1.1$ | |
| $kT_{\rm e}$ (keV) | $32.4^{+5.5}_{-3.5}$ | $15.2^{+3.4}_{-2.5}$ | $31.3^{+3.9}_{-2.9}$ | | $18.2^{+8.0}_{-3.5}$ |
| refl$_{\rm frac}$ | $8.8^{+3.5}_{-2.7} \times 10^{-2}$ | $0.51^{+0.13}_{-0.11}$ | $0.10^{+0.04}_{-0.01}$ | | $0.45^{+0.12}_{-0.16}$ |
| Norm ($10^{-4}$) | $21.8 \pm 0.8$ | $7.2 \pm 0.3$ | $21.6 \pm 0.9$ | | $7.5 \pm 0.4$ |
| $C_{\rm FPMA/LAXPC}$ | 1 (fixed) | 1 (fixed) | 1 (fixed) | | 1 (fixed) |
| $C_{\rm NICER}$ | $0.925 \pm 0.004$ | $1.13 \pm 0.02$ | $0.927 \pm 0.005$ | | $1.13 \pm 0.02$ |
| $C_{\rm FPMB/SXT}$ | $0.992 \pm 0.002$ | $1.16 \pm 0.02$ | $0.992 \pm 0.003$ | | $1.16 \pm 0.02$ |
| Flux$_{0.1-100\ \rm keV}$[b] | $1.96 \times 10^{-9}$ | $6.9 \times 10^{-10}$ | $1.94 \times 10^{-9}$ | | $7.2 \times 10^{-10}$ |
| $L_{0.1-100\ \rm keV}$[c] | $2.87 \times 10^{36}$ | $1.01 \times 10^{36}$ | $2.84 \times 10^{36}$ | | $1.05 \times 10^{36}$ |
| $\chi^2$/dof | 592.5/610 | 749.8/679 | | 1257/1293 | |

**Notes.** All errors and upper limits reported in this table are at a 90% confidence level ($\Delta\chi^2 = 2.7$).
[a] The emission radius is calculated assuming a distance of 3.5 kpc.
[b] Unabsorbed flux in units of erg cm$^{-2}$ s$^{-1}$.
[c] X-ray Luminosity in units of erg s$^{-1}$.

evolves, with $\Gamma$ increasing from $\sim$1.88 to $\sim$1.99 and the electron temperature decreasing from $\sim$31 to $\sim$18 keV. The blackbody temperature exhibits a mild decrease, accompanied by a reduction in normalization. The reflection modeling suggests a common inclination of $\sim$39° and an iron abundance of $A_{\rm Fe} \sim 3.3$. The normalization of the reflection component also decreases, consistent with the overall decline in flux. refl$_{\rm frac}$, which is defined as the ratio of the intensity illuminating the disk to the intensity reaching the observer or infinity (T. Dauser et al. 2016), increased from $\sim$0.1 to $\sim$0.45. The unabsorbed flux drops from $\sim 2 \times 10^{-9}$ to $\sim 7 \times 10^{-10}$ erg cm$^{-2}$ s$^{-1}$, corresponding to a luminosity decrease from $2.8 \times 10^{36}$ to $1 \times 10^{36}$ erg s$^{-1}$ (assuming a distance of 3.5 kpc; D. K. Galloway et al. 2005).

## 4. Discussion

SAX J1808.4–3658 was observed in its tenth known outburst in 2022. We report results from our broadband timing and spectral study of SAX J1808.4–3658 based on NuSTAR and AstroSat observations performed near the peak (Epoch 1) and decay phase (Epoch 2) of the outburst, respectively, simultaneously with NICER. Our joint analysis of NICER, NuSTAR, and AstroSat observations provides a comprehensive insight

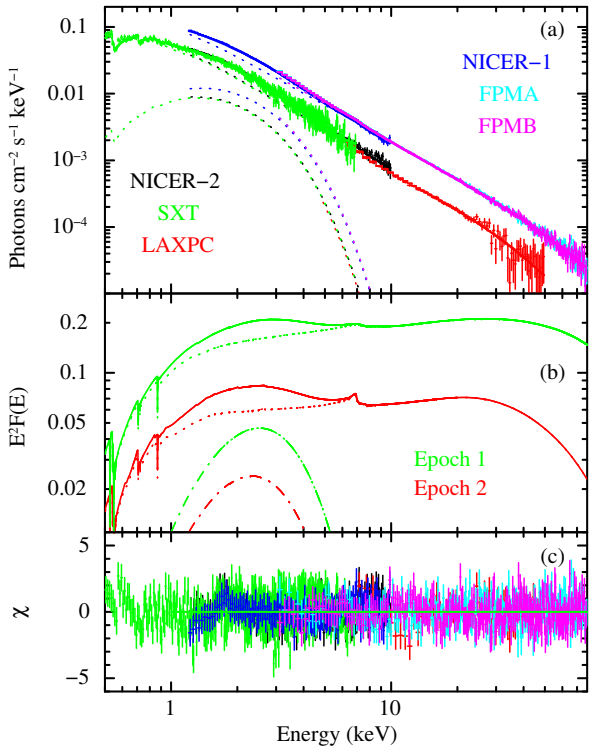


**Figure 6.** Joint broadband spectral fit of SAX J1808.4–3658 using NuSTAR (Epoch 1) and AstroSat (Epoch 2), together with simultaneous NICER coverage. The spectra are modeled with `tbabs*(bbodyard + relxillCP)`. (a) Observed spectra with the best-fit model. (b) Comparison of the emission model for both epochs, showing the contributions from the blackbody emission (dashed–dotted lines) and the `relxillCP` component (dotted lines). (c) Residuals with respect to the best-fit model.

into the evolution of the pulse properties and broadband spectrum over these two distinct stages.

### 4.1. Timing Properties

The coherent pulsations at ∼401 Hz were detected throughout both epochs, confirming the persistent channeling of accretion flow onto the magnetic poles during the outburst. Pulse timing results obtained are compatible within the errors with the solution obtained with NICER (G. Illiano et al. 2023). The pulse profiles in the energy band 3–30 keV from both epochs are well described by two harmonically related sinusoidal components, with the fundamental amplitude increasing from ∼4% near the outburst peak to ∼6% during the decay. Notably, during the reflaring stage of the 2022 outburst, the fundamental amplitude was reported to reach even higher values, up to ∼10% during the low-flux state (C. Ballocco et al. 2025a). This increase likely reflects changes in the accretion column geometry or hotspot visibility as the accretion rate declines (J. J. E. Kajava et al. 2011; I. D. Markozov & A. A. Mushtukov 2024). The harmonic content remains broadly similar between epochs in the hard X-ray band, although a weak third harmonic component may be present, albeit with low significance.

### 4.2. Energy Dependence of Pulsed Emission

The fractional amplitude and phase lag were found to be energy-dependent during this outburst, similar to previous outbursts (e.g., J. M. Hartman et al. 2009; A. Sanna et al. 2017; P. Bult et al. 2020; R. Sharma et al. 2023). We checked for the energy dependence in the 0.5–30 keV range. During both epochs, the fundamental amplitude increases with energy up to ∼3 keV before decreasing at higher energies. The peak fractional amplitude reached ∼7% during Epoch 1, while it peaked around 9% for Epoch 2. Similar trends were also observed with XMM-Newton observation taken during the reflaring phase (C. Ballocco et al. 2025a). The harmonic component in Epoch 1 increased steadily with energy, reaching ∼2% at the higher energies, while the harmonic became more prominent above 5 keV in Epoch 2, reaching ∼3% at higher energies. A similar trend of increase in the fractional amplitude of the harmonic with energy has been observed in the previous outburst of 2019 (P. Bult et al. 2020; R. Sharma et al. 2023). However, the energy dependence of the fractional amplitudes varies considerably between different outbursts and luminosities (e.g., J. M. Hartman et al. 2009; A. Patruno et al. 2009; A. Sanna et al. 2017; P. Bult et al. 2020). During Epoch 1, a dip feature in the fractional amplitude around the 6–7 keV energy range (corresponding to the Fe line) is evident, which is absent from Epoch 2. A similar drop in fractional amplitude near the Fe line was previously observed during the 2008 and 2015 outbursts (A. Patruno et al. 2009; A. Sanna et al. 2017), whereas no such feature was seen in the 2019 outburst (R. Sharma et al. 2023).

The time lags during the 2022 outburst exhibited the typical behavior seen in SAX J1808.4–3658. The hard photons arrive earlier than soft ones, producing a negative lag that increases with energy (e.g., W. Cui et al. 1998; M. Gierliński et al. 2002; J. M. Hartman et al. 2009; A. Ibragimov & J. Poutanen 2009; R. Sharma et al. 2023). In both epochs, the fundamental component exhibited soft lags reaching 0.2–0.3 ms. The harmonic component showed a similar order of lag in Epoch 2, while no significant lag was observed during Epoch 1. The time lags in SAX J1808.4–3658 are known to depend on source flux, typically becoming more pronounced as the accretion rate decreases. Soft lags in the fundamental component are observed throughout the outburst's evolution, while lags for harmonics are less pronounced or become hard lags at higher luminosities (J. M. Hartman et al. 2009; A. Ibragimov & J. Poutanen 2009). During the 2019 outburst, both the fundamental and harmonic components showed lags of comparable magnitude but with the opposite trend when observed near the outburst peak with AstroSat (R. Sharma et al. 2023). These lags can be explained by the model where the soft thermal emission and Comptonization emissivity (or beaming) patterns are different, each affected differently by rapid stellar rotation (M. Gierliński et al. 2002; J. Poutanen & M. Gierliński 2003; A. Ibragimov & J. Poutanen 2009). The stronger pulsation amplitude and persistent negative lags in Epoch 2 suggest a reduction in scattering depth and a more compact emission geometry as the outburst decayed (J. Poutanen 2004; K. Viironen & J. Poutanen 2004; M. Falanga & L. Titarchuk 2007; A. A. Mushtukov & S. Portegies Zwart 2023).

### 4.3. Spectral Properties

The broadband X-ray spectrum of SAX J1808.4–3658 in both epochs is well described by the combination of a soft thermal component, a Comptonized continuum, and a significant relativistic reflection component from the accretion disk. A joint fit to the spectra from both epochs, with linked parameters expected to remain unchanged, reinforces the

trends inferred from the individual fits. A common inclination ($\sim$39°) and iron abundance ($A_{\rm Fe} \sim 3.3$) were observed. We observe pronounced spectral evolution between the two epochs. The X-ray luminosity decreases by a factor of $\sim$3 from Epoch 1 to Epoch 2, reflecting the declining accretion rate. The Comptonized continuum softens, with the photon index increasing from $\Gamma \sim 1.88$ to $\Gamma \sim 1.99$, while the electron temperature decreases from $\sim$31 to $\sim$18 keV. These changes indicate enhanced Compton cooling as the accretion rate falls. The ionization parameter drops from $\log \xi \sim 3.4$ to $\log \xi \sim 1.8$, and the reflection fraction increases, suggesting that as the disk cools and becomes less ionized, a larger fraction of the Comptonized flux is intercepted and reprocessed by the disk (P. O. Petrucci et al. 2001; J. García & T. R. Kallman 2010).

Although spectral softening is evident between Epochs 1 and 2, the best-fitting spectral parameters indicate that SAX J1808.4–3658 remained in the hard spectral state during both epochs. The hardness ratio measured with NuSTAR and AstroSat showed a significant decrease between the two epochs, while the NICER data reveal only a mild downward trend. This reduction in hardness is consistent with the spectral softening inferred from our broadband fits, likely reflecting changes in the Comptonizing plasma and disk emission as the outburst evolves (J. Poutanen & M. Gierliński 2003; M. Falanga et al. 2005; C. Ferrigno et al. 2017; A. Patruno & A. L. Watts 2021). Despite this evolution, no evidence for a transition to a soft state is observed in the 2022 outburst, similar to the behavior reported during the 2019 event. In contrast, during the 2015 outburst, T. Di Salvo et al. (2019) reported the state transition in SAX J1808.4–3658 with XMM-Newton (soft state) and NuSTAR (hard state) observations.

### 4.4. Comparison with Other Studies of the 2022 Outburst

Several studies have reported results from the 2022 outburst of SAX J1808.4–3658 using different instrumental combinations and scientific focuses. In particular, A. Kaushik et al. (2025) and K. Bruce et al. (2026) investigated the broadband spectral properties using NICER in combination with hard X-ray observations, while C. Ballocco et al. (2025a) focused on the temporal and spectral behavior during the reflaring phase using XMM-Newton and HST data. In addition, B. Dorsman et al. (2026) modeled the pulse profiles from NICER to constrain the emission geometry. While these works employ broadly similar spectral components, our analysis provides complementary and, in several respects, new insights into the 2022 outburst.

The main differences and advances of the present work can be summarized as follows:

1. Our analysis exploits strictly simultaneous broadband coverage, combining NICER with NuSTAR (Epoch 1) and AstroSat (Epoch 2), and explicitly tracks the evolution of both pulsed and spectral properties between the peak and decay phases of the outburst.
2. Our work also extends previous work by incorporating a detailed timing analysis and energy-resolved pulse properties. For the first time for the 2022 outburst, we report the energy dependence of the pulsed fractional amplitude and phase lags across two distinct outburst phases: the peak and decay phases. The detection of epoch-dependent changes in harmonic content, the presence of a dip in the fractional amplitude of the fundamental at the Fe-line energy during the peak, and the evolution of soft lags provide new constraints on the geometry of the emission regions that were not addressed in previous studies.
3. K. Bruce et al. (2026) performed broadband spectral modeling using a single NICER observation closest in time to the corresponding NuSTAR exposure. In contrast, we explicitly merged multiple NICER observations to construct event files that strictly overlap the NuSTAR and AstroSat time windows. This approach captures intrinsic flux variability within each broadband observation and yields a more representative description of the instantaneous spectral state, which is particularly important given the rapid evolution in luminosity observed during the 2022 outburst.
4. From a spectral perspective, our joint fitting of Epochs 1 and 2 allows us to track the intraoutburst evolution of spectral parameters in a self-consistent manner. While K. Bruce et al. (2026) constrained reflection parameters by jointly fitting the 2019 and 2022 outbursts, our analysis focuses specifically on the evolution within the 2022 outburst itself. Our results suggest a dynamically changing corona–disk coupling on timescales of days, complementing the longer-term comparisons presented in earlier works. Although broadly similar continuum and relativistic reflection models are employed, differences are observed between our results and those of K. Bruce et al. (2026), particularly in the inferred inclination, disk ionization, and reflection fraction. These discrepancies are likely attributable to differences in modeling approaches. For instance, we allowed the iron abundance to vary freely, finding values higher than solar, and we did not model the $\sim$1 keV feature, which can influence the reflection continuum at low energies.
5. A. Kaushik et al. (2025) classified the source as being in a soft spectral state throughout the 2022 outburst. This interpretation differs from our results, which indicate that SAX J1808.4–3658 remained in the hard state during both epochs. Our conclusion is based on broadband spectral modeling extending up to $\sim$50–78 keV, which provides stronger constraints on the Comptonized continuum and high-energy cutoff, and is consistent with the findings of K. Bruce et al. (2026) and C. Ballocco et al. (2025a). The discrepancy likely arises from differences in the spectral approach and energy coverage, as A. Kaushik et al. (2025) based their classification primarily on modeling of the NICER data. In addition, A. Kaushik et al. (2025) reported fractional rms amplitude of red noise components in the range of $\sim$12%–26%, which are characteristic of NS-LMXBs in the hard state, where rms values of $\gtrsim$10%–20% are typically observed (see, e.g., T. Muñoz-Darias et al. 2014; R. Sharma et al. 2023; R. Sharma 2025).
6. In other studies of the 2022 outburst, the $\sim$1 keV feature detected in NICER spectra was modeled using an additional Gaussian component (A. Kaushik et al. 2025; K. Bruce et al. 2026; B. Dorsman et al. 2026), as similar features were reported during earlier outbursts (e.g., R. Sharma et al. 2023). However, during the 2022 outburst, we did not include this feature in our spectral modeling, as it is not detected with AstroSat/SXT and

may be affected by instrumental background effects or uncertainties in the NICER effective area (see, e.g., H. Hall et al. 2025). Moreover, if this feature were intrinsic to the source and originated from the same region and/or ionization state as the Fe K emission, it would be expected to be reproduced by a self-consistent reflection model, which is not observed (K. Bruce et al. 2026).

7. The presence of a soft thermal component with a temperature of ∼0.6 keV and an emitting radius of ∼2–3 km is broadly consistent with previous findings. C. Ballocco et al. (2025a) reported a similar size of emitting region during the reflaring phase, albeit with a lower temperature of ∼0.36 keV, likely reflecting cooler thermal emission associated with a lower accretion rate.

At the time of writing, no refereed publications are available for the 2025 outburst of SAX J1808.4–3658. Preliminary reports suggest comparable peak luminosities with a broadly similar outburst morphology (C. Ballocco et al. 2025b, 2025c), but no detailed broadband timing or reflection-based spectral analysis has yet been presented. Our results from the 2022 outburst, therefore, provide a valuable reference framework for interpreting future observations of the 2025 outburst, particularly in assessing whether similar coronal cooling, evolution of reflection, and pulse-lag behavior recur across successive outbursts.

## 5. Conclusions

We have presented a detailed timing and broadband spectral investigation of the AMXP SAX J1808.4–3658 during its 2022 outburst, based on coordinated observations with NICER, NuSTAR, and AstroSat covering both the peak and decay phases. Our main findings can be summarized as follows:

1. Coherent pulsations at ∼401 Hz persist throughout the outburst, with the pulsed fractional amplitude of the fundamental increasing from the peak to the decay phase and an evolving harmonic component as the accretion rate declines.
2. The energy dependence of the pulse amplitude and time lags exhibits clear epoch-dependent behavior, including a transient dip at the Fe-line energy during the outburst peak.
3. The broadband spectrum shows pronounced evolution, with spectral softening, a decrease in coronal electron temperature, and a reduction in disk ionization as the accretion rate declines. This behavior is consistent with gradual spectral softening within the hard state rather than a full state transition.
4. An increasing reflection fraction during the decay phase suggests a more compact corona and enhanced disk covering fraction at lower accretion rates.
5. The combined timing and spectral results point to a coupled evolution of the corona, accretion disk, and magnetosphere as the system transitions from the peak to the decay phase of the outburst.

Overall, our analysis demonstrates the importance of strictly simultaneous broadband coverage and joint timing and spectral diagnostics in disentangling the physical processes governing AMXPs. The results place the 2022 outburst of SAX J1808.4–3658 in the broader context of its recurrent activity and provide a robust reference for forthcoming detailed studies of the 2025 outburst.

## Acknowledgments

This research has made use of AstroSat data, obtained from the Indian Space Science Data Centre (ISSDC), and NuSTAR and NICER data obtained from the High Energy Astrophysics Science Archive Research Center (HEASARC). We thank the LAXPC Payload Operation Center (POC) and the SXT POC at TIFR, Mumbai, for providing the necessary software tools. We thank the anonymous referee for constructive comments and suggestions.

*Facilities:* NICER, NuSTAR, AstroSat.

*Software*: Heasoft, Xspec.

## Appendix
## Pulse Profile Shape

The pulse profiles shown in Figure 2 appear slightly offset from the baseline level of unity and are not symmetrically distributed around it. This effect is more pronounced in the NuSTAR and AstroSat profiles. The apparent offset arises from the combined contribution of the fundamental and harmonic components to the total pulse shape. While the individual fundamental and harmonic components are each symmetric about the baseline level of unity, their superposition produces an asymmetric total profile.

Figure 7 illustrates this effect by showing the individual contributions of the fundamental and harmonic components, along with their combined pulse profile. In particular, the harmonic component contributes additional flux near the pulse maximum as well as at other pulse phases, leading to an enhanced peak and a shallower minimum. As a result, the total pulse profile spans an asymmetric range due to the relative phase alignment between the harmonic and fundamental components.

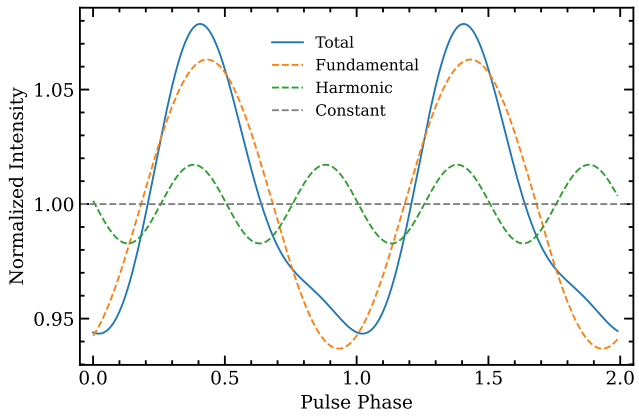


**Figure 7.** Decomposition of the LAXPC pulse profile into its fundamental and harmonic components. The individual components are symmetric about the baseline level of unity, while their superposition produces an asymmetric total pulse profile due to their relative phase alignment.

## ORCID iDs

Rahul Sharma https://orcid.org/0000-0003-0366-047X
Andrea Sanna https://orcid.org/0000-0002-0118-2649
Prince Sharma https://orcid.org/0000-0003-4696-940X

## References

Agrawal, P. C. 2006, AdSpR, 38, 2989
Ambrosino, F., Miraval Zanon, A., Papitto, A., et al. 2021, NatAs, 5, 552
Antia, H. M., Yadav, J. S., Agrawal, P. C., et al. 2017, ApJS, 231, 10
Arnaud, K. A. 1996, ASPC, 101, 17
Baglio, M. C., Russell, D. M., Alabarta, K., et al. 2022, ATel, 15603, 1
Baglio, M. C., Russell, D. M., Crespi, S., et al. 2020, ApJ, 905, 87
Ballocco, C., Papitto, A., Miraval Zanon, A., et al. 2025a, arXiv:2506.19556
Ballocco, C., Papitto, A., Zanon, A. M., Illiano, G., & Ambrosino, F. 2025b, ATel, 17326, 1
Ballocco, C., Trois, A., Papitto, A., et al. 2025c, ATel, 17369, 1
Beri, A., Sharma, R., Roy, P., et al. 2023, MNRAS, 521, 5904
Braje, T. M., Romani, R. W., & Rauch, K. P. 2000, ApJ, 531, 447
Bruce, K., Tsuruta, S., Liebmann, A. C., & Teter, M. 2026, ApJ, 996, 73
Bult, P., Altamirano, D., Arzoumanian, Z., et al. 2022, ApJL, 935, L32
Bult, P., Chakrabarty, D., Arzoumanian, Z., et al. 2020, ApJ, 898, 38
Burderi, L., Di Salvo, T., Lavagetto, G., et al. 2007, ApJ, 657, 961
Cackett, E. M., Altamirano, D., Patruno, A., et al. 2009, ApJL, 694, L21
Cackett, E. M., Miller, J. M., Ballantyne, D. R., et al. 2010, ApJ, 720, 205
Chakrabarty, D., & Morgan, E. H. 1998, Natur, 394, 346
Cui, W., Morgan, E. H., & Titarchuk, L. G. 1998, ApJ, 504, L27
Dauser, T., Garcia, J., Parker, M. L., Fabian, A. C., & Wilms, J. 2014, MNRAS, 444, L100
Dauser, T., García, J., Walton, D. J., et al. 2016, A&A, 590, A76
Di Salvo, T., & Sanna, A. 2022, ASSL, 465, 87
Di Salvo, T., Sanna, A., Burderi, L., et al. 2019, MNRAS, 483, 767
Dorsman, B., Salmi, T., Watts, A. L., et al. 2026, MNRAS, 545, staf1983
Fabian, A. C., & Ross, R. R. 2010, SSRv, 157, 167
Falanga, M., Bonnet-Bidaud, J. M., Poutanen, J., et al. 2005, A&A, 436, 647
Falanga, M., & Titarchuk, L. 2007, ApJ, 661, 1084
Ferrigno, C., Bozzo, E., Sanna, A., et al. 2017, MNRAS, 466, 3450
Galloway, D. K., Wang, Z., & Morgan, E. H. 2005, ApJ, 635, 1217
García, J., Dauser, T., Lohfink, A., et al. 2014, ApJ, 782, 76
García, J., & Kallman, T. R. 2010, ApJ, 718, 695
García, J. A., Steiner, J. F., Grinberg, V., et al. 2018, ApJ, 864, 25
Gendreau, K. C., Arzoumanian, Z., Adkins, P. W., et al. 2016, SPIE, 9905, 99051H
Gierliński, M., Done, C., & Barret, D. 2002, MNRAS, 331, 141
Goodwin, A. J., Russell, D. M., Galloway, D. K., et al. 2020, MNRAS, 498, 3429
Hall, H., Ludlam, R. M., Miller, J. M., et al. 2025, ApJ, 980, 234
Harrison, F. A., Craig, W. W., Christensen, F. E., et al. 2013, ApJ, 770, 103
Hartman, J. M., Patruno, A., Chakrabarty, D., et al. 2009, ApJ, 702, 1673
Hasinger, G., & van der Klis, M. 1989, A&A, 225, 79
Ibragimov, A., & Poutanen, J. 2009, MNRAS, 400, 492
Illiano, G., Papitto, A., Sanna, A., et al. 2023, ApJL, 942, L40
Illiano, G., Papitto, A., Zanon, A. M., et al. 2022, ATel, 15647, 1
Imai, Y., Serino, M., Negoro, H., et al. 2022, ATel, 15563, 1
Kaastra, J. S., & Bleeker, J. A. M. 2016, A&A, 587, A151
Kajava, J. J. E., Ibragimov, A., Annala, M., Patruno, A., & Poutanen, J. 2011, MNRAS, 417, 1454
Kaushik, A., Bhargava, Y., Bhattacharyya, S., & Falanga, M. 2025, ApJ, 993, 140
Ludlam, R. M., Miller, J. M., Degenaar, N., et al. 2017, ApJ, 847, 135
Markozov, I. D., & Mushtukov, A. A. 2024, MNRAS, 527, 5374
Muñoz-Darias, T., Fender, R. P., Motta, S. E., & Belloni, T. M. 2014, MNRAS, 443, 3270
Mukherjee, D., Bult, P., van der Klis, M., & Bhattacharya, D. 2015, MNRAS, 452, 3994
Mushtukov, A. A., & Portegies Zwart, S. 2023, MNRAS, 518, 5457
Ng, M., Ray, P. S., Bult, P., et al. 2021, ApJL, 908, L15
Papitto, A., Di Salvo, T., D'Aì, A., et al. 2009, A&A, 493, L39
Patruno, A., Jaodand, A., Kuiper, L., et al. 2017, ApJ, 841, 98
Patruno, A., Rea, N., Altamirano, D., et al. 2009, MNRAS, 396, L51
Patruno, A., & Watts, A. L. 2021, ASSL, 461, 143
Petrucci, P. O., Merloni, A., Fabian, A., Haardt, F., & Gallo, E. 2001, MNRAS, 328, 501
Poutanen, J. 2004, AIPC, 714, 228
Poutanen, J., & Gierliński, M. 2003, MNRAS, 343, 1301
Remillard, R. A., Loewenstein, M., Steiner, J. F., et al. 2022, AJ, 163, 130
Russell, D. M., Alabarta, K., Saikia, P., et al. 2025, ATel, 17323, 1
Sanna, A., Bult, P., Ng, M., et al. 2022a, MNRAS, 516, L76
Sanna, A., Bult, P. M., Gendreau, K. C., et al. 2022b, ATel, 15559, 1
Sanna, A., Di Salvo, T., Burderi, L., et al. 2017, MNRAS, 471, 463
Sharma, R. 2025, JHEAp, 47, 100376
Sharma, R., Beri, A., Sanna, A., & Dutta, A. 2020, MNRAS, 492, 4361
Sharma, R., Jain, C., & Dutta, A. 2019, MNRAS, 482, 1634
Sharma, R., Sanna, A., & Beri, A. 2023, MNRAS, 519, 3811
Singh, K. P., Stewart, G. C., Chandra, S., et al. 2016, SPIE, 9905, 99051E
Singh, K. P., Stewart, G. C., Westergaard, N. J., et al. 2017, JApA, 38, 29
Singh, K. P., Tandon, S. N., Agrawal, P. C., et al. 2014, SPIE, 9144, 91441S
Srinivasan, G. 2010, NewAR, 54, 93
Viironen, K., & Poutanen, J. 2004, A&A, 426, 985
Wijnands, R., & van der Klis, M. 1998, Natur, 394, 344
Wilkins, D. R., & Fabian, A. C. 2012, MNRAS, 424, 1284
Wilms, J., Allen, A., & McCray, R. 2000, ApJ, 542, 914
Yadav, J. S., Agrawal, P. C., Antia, H. M., et al. 2016, SPIE, 9905, 99051D
Zdziarski, A. A., Johnson, W. N., & Magdziarz, P. 1996, MNRAS, 283, 193